PCCP

Accepted Manuscript

ROYAL SOCIETY OF CHEMISTRY

www.rsc.org/pccp

Physical Chemistry Chemical Physics
CREATED USING THE RSC LaTeX PCCP ARTICLE TEMPLATE – SEE www.rsc.org/electronicfiles FOR DETAILS
ARTICLE TYPE www. rsc.org/xxxxxx | XXXXXXXX

Anharmonicities and coherent vibrational dynamics of phosphate ions in bulk H_2O

Rene Costard,*[a] Tobias Tyborski,[a] and Benjamin P. Fingerhut*[a]

Received Xth XXXXXXXXXX 2015, Accepted Xth XXXXXXXXX 20XX
First published on the web Xth XXXXXXXXXX 200X
DOI: 10.1039/b000000x

Phosphates feature prominently in the energetics of metabolism and are important solvation sites of DNA and phospholipids. Here we investigate the ion $H_2PO_4^-$ in aqueous solution combining 2D IR spectroscopy of phosphate stretching vibrations in the range from 900-1300 cm^{-1} with ab-initio calculations and hybrid quantum-classical molecular dynamics based simulations of the non-linear signal. While the line shapes of diagonal peaks reveal ultrafast frequency fluctuations on a sub-100 fs timescale caused by the fluctuating hydration shell, an analysis of the diagonal and cross-peak frequency positions allows for extracting inter-mode couplings and anharmonicities of 5–10 cm^{-1}. The excitation with spectrally broad pulses generates a coherent superposition of symmetric and asymmetric PO_2^- stretching modes resulting in the observation of a quantum beat in aqueous solution. We follow its time evolution through the time-dependent amplitude and shape of the cross peaks. The results provide a complete characterization of the $H_2PO_4^-$ vibrational Hamiltonian including fluctuations induced by the native water environment.

1 Introduction

Biomolecules like DNA, phospholipids, and adenosine triphosphate (ATP) contain phosphate groups as essential building blocks[1,2] and hydration hotspots[3–5]. The phosphate ion $H_2PO_4^-$ plays a prominent role as intermediate in the regulation of signal transduction, e.g., by guanosine triphosphate hydrolysis[6,7]. While the equilibrium structures of these systems have been well characterized[8–11], an understanding of their biological function requires the knowledge of their microscopic interactions with the fluctuating environment through electric fields and hydrogen bonding, i.e., the ultrafast dynamics on the femto- to picosecond time scale of molecular motions. Two-dimensional infrared (2D IR) spectroscopy which combines chemical selectivity with a (sub-)100 fs time resolution and computer simulations have been successfully applied to study these phenomena in water[12–14], DNA[15–17], proteins[18–21] and ion-water interactions[22–27]. The results show that the understanding of intra- and intermolecular couplings provides unique insight into structural dynamics and energy relaxation pathways.

We have recently introduced the phosphate ion $H_2PO_4^-$ as a model system to study ultrafast phosphate dynamics combining two advantages: i) interfacial sensitivity of phosphate stretching vibrations allowing for direct observation of phosphate-water interactions in bulk H_2O, and ii) small molecular structure making them tractable for realistic state of the art simulations[28]. 2D IR spectra of PO_2^- stretching vibrations together with a QM:MM instantaneous normal mode (INM) analysis revealed predominantly homogeneously broadened lines due to fast sub-100 fs librational motions of hydration-shell water in striking contrast to inhomogeneously broadened bands in DNA and phospholipids[29,30].

Here we analyze 2D spectra recorded in an extended 870-1300 cm^{-1} frequency range which cover the PO_2^- stretching, $P(OH)_2$ stretching and $P(OH)_2$ bending modes of $H_2PO_4^-$ in H_2O solvent. The experimental signals are analyzed with help of an ab-initio derived model used to simulate linear IR (Sec. 2.1) and respective absorptive 2D IR spectra (Sec. 2.2). This analysis provides insight into the molecular Hamiltonian determined by the $H_2PO_4^-$ multidimensional potential and ultrafast phosphate-water interactions (Sec. 2.2.1), information not accessible with linear spectroscopy. By constructing the bi-exciton Hamiltonian, we find small inter-mode couplings and anharmonicities (Sec. 2.2.2) with the exception of a Fermi-resonance where redistribution of oscillator strength within bi-excitons leads to anomalous line shapes in 2D signals induced by substantial mode mixing of phosphate stretching with low-frequency skeleton modes (Sec. 2.2.3). The analysis of cross-peak dynamics during the waiting time T reveals

† Electronic Supplementary Information (ESI) available: $H_2PO_4^- \times xH_2O$ cluster geometries; Pump-probe data; Simulation details of nonlinear response function; Coherent wave packet dynamics; IR frequencies of the $H_2PO_4^-$ *$5H_2O$ water cluster See DOI: 10.1039/b000000x/

[a] *Max-Born-Institut für Nichtlineare Optik und Kurzzeitspektroskopie, Max-Born-Str. 2A, D-12489 Berlin, Germany. E-mail: costard@mbi-berlin.de, fingerhut@mbi-berlin.de*

signatures of a coherent vibrational quantum beat (Sec. 2.2.4).

2 Results and Discussion:

2.1 Linear absorption of $H_2PO_4^-$:

Phosphate stretching vibrations of $H_2PO_4^-$ ions in aqueous solution cover the range from 850 to 1300 cm^{-1} (cf. Fig. 1a). While the symmetric and asymmetric PO_2^- stretching vibrations ($\nu_S(PO_2^-)$ and $\nu_{AS}(PO_2^-)$) are found at 1080 and 1160 cm^{-1}, the P-$(OH)_2$ stretching vibrations (ν_S(P-$(OH)_2$) and $\nu_{AS}(P(OH)_2)$) occur at significantly lower frequencies of 880 and 940 cm^{-1}. The stretching vibrations are complemented by bending vibrations of the hydroxyl groups (δ(P-$(OH)_2$)) which occur as a high-frequency shoulder at 1250 cm^{-1}.

For the theoretical analysis of the $H_2PO_4^-$ vibrational structure, $H_2PO_4^-$/water clusters ($H_2PO_4^- \times xH_2O$) are designed to cover all H-bond coordination sites of the solute $H_2PO_4^-$, i.e., PO_2^- H-bond acceptor sites and P-OH H-bond donor sites. In Ref. 28 the sensitivity of $H_2PO_4^-$ vibrational modes to the surrounding solvation shell and associated induced frequency shifts were demonstrated, showing a pronounced blue/red shift of $\nu_{AS}(P(OH)_2)/\nu_{AS}(PO_2^-)$ with increasing hydration as well as a coupling of the PO_2^- stretching and the P-$(OH)_2$ bending modes. These predictions were recently confirmed experimentally[31]. The role of the bending modes is further investigated by deuteration experiments (Fig. 1a, dashed line) showing a disappearance of the high-frequency shoulder at 1250 cm^{-1} and an appearance of a low-frequency shoulder at 900 cm^{-1} that is assigned to the P-$(OD)_2$ bending vibrations. In parallel, the PO_2^- stretching modes shift toward higher frequencies due to a change in mode character

Here, we provide complementary information starting from a local mode perspective[32,33] and demonstrate how the relevant couplings and anharmonic corrections transform into the spectroscopic basis. Without symmetry restrictions a minimum structure for a cluster with seven water molecules ($H_2PO_4^- \times 7H_2O$) was located on the first-principles level of theory (PBE0/6-311++G**) and confirmed by normal mode analysis. The normal mode frequencies of the $H_2PO_4^-$ are depicted in Fig. 1b, middle (dashed lines, explicit values are given in Table 1, geometries of clusters are depicted in Fig. S1, ESI†). A comparison of normal and local mode frequencies (Fig. 1b, right) reveals that the δ(P-(OH)) modes are only slightly shifted and the splitting of local δ(P-(OH)) modes is preserved due to the asymmetric H_2O environment in the $H_2PO_4^- \times 7H_2O$ cluster. In contrast the two local oscillators of PO_2^- (ν(P=O)) appear at similar frequencies (1109/1077 cm^{-1}) while the local ν(P-(OH)) stretching modes are nearly degenerate (876/874 cm^{-1}). This result suggests a bilinear coupling of 36 cm^{-1} for ν(P=O), and 42 cm^{-1} for ν(P-(OH)) in the solvated cluster, obtained from diagonalizing a local mode Hamiltonian of ν(P=O) and ν(P-(OH)) stretching modes under the assumption of idealized pairwise bilinear coupling of respective local modes. We note that this assumption is justified for ν(P-(OH)), whereas the microscopic origin of the ν(P=O) frequency position is more complex due to mode mixing with δ(P-(OH)) modes[28]. Inter-mode couplings of normal modes are significantly smaller than in the local mode representation (see below). As such, delocalized normal modes with elongations involving multiple bonds will be used in the following.

The anharmonic corrections to fundamental v=0→1 transitions are evaluated on the vibrational configuration interaction / vibrational self consistent field (*VCI/VSCF*) level of theory[34–39] that is briefly described in Sec. 5 (compare dashed and solid lines in Fig. 1b, middle; Table 1). Results of the *VCI/VSCF* method serve twofold in the current study: first anharmonic corrections of fundamental transitions provide a benchmark for the quality of harmonic frequencies of $H_2PO_4^-$. Second, anharmonicities of combination and overtone bands of phosphate modes are employed for the construction of the bi-exciton Hamiltonian used in the simulation of 2D IR spectra of $H_2PO_4^-$, which provide information not directly accessible in linear absorption spectra (cf. Sec. 2.2).

Compared to the harmonic frequencies, the sophisticated VCI level of theory induces a minor red shift on the order of 13-16 cm^{-1} for $\nu_{AS/S}(PO_2^-)$ which is negligible for ν_{AS}(P-$(OH)_2$) (1-2 cm^{-1}). We find that both, the $\nu_{AS/S}(PO_2^-)$ and $\nu_{AS/S}$(P-$(OH)_2$) modes of the $H_2PO_4^- \times 7H_2O$ cluster appear below the experimental values. This behavior is assigned to an overbinding of the central $H_2PO_4^-$ ion with the surrounding H_2O molecules due to the absence of a second solvation shell. Hybrid QM/MM simulations (Fig. 1b, left), where extended solvent interactions are accounted for on a classical level of theory, allow to obtain good agreement with the experiment which further supports this assignment.

Overall we find that the phosphate modes of $H_2PO_4^-$ are adequately described in the harmonic approximation, i.e., the harmonic reference system provides a good zero-order Hamiltonian with small anharmonic corrections. These anharmonic corrections mainly arise from even order coupling terms (quartic) of the potential energy function. This is in contrast to high-frequency O-H stretch vibrations of $H_2PO_4^-$ (cf. Fig. 1c and Table 1) and bulk water[40] where odd order corrections dominate anharmonic corrections of v=0→1 transitions and thus render the harmonic reference frame a zero-order Hamiltonian of moderate quality.

In Fig. 1a we present the simulated linear absorption spectrum of $H_2PO_4^-$ (red line) where we parametrize the model, i.e. frequency positions and line shapes, from ab-initio data. Fundamental v=0→1 transitions are obtained from averaging over instantaneous frequencies of hybrid QM/MM simulations. The line shapes determined by Gaussian frequency

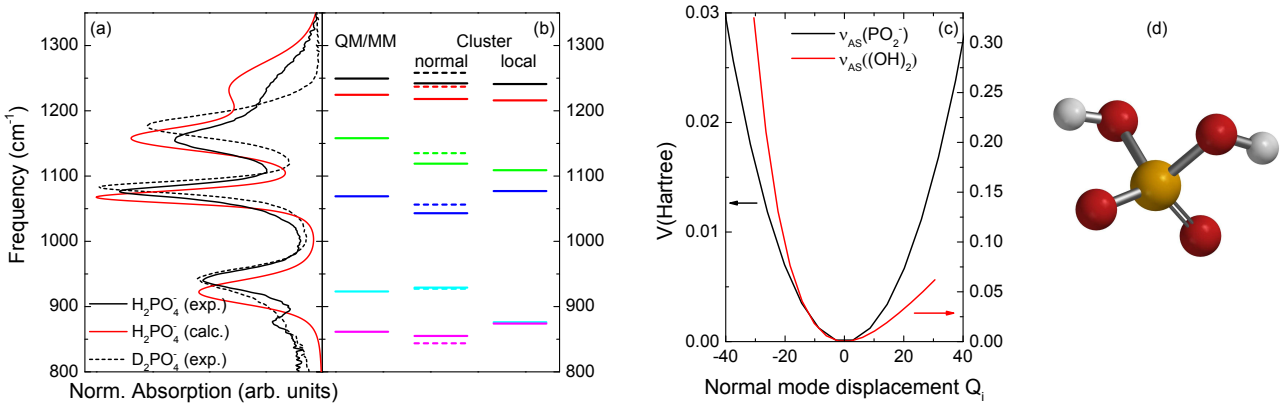

Fig. 1 (a) Comparison of the experimental (black) and simulated (red) linear absorption of $H_2PO_4^-$, experimental spectrum of $D_2PO_4^-$ is shown as dashed line; (b) Frequency values of (from top to bottom) δ_{AS}(P-(OH)$_2$) (black), δ_S(P-(OH)$_2$) (red), $\nu_{AS}(PO_2^-)$ (green), $\nu_S(PO_2^-)$ (blue), ν_{AS}(P-(OH)$_2$) (cyan) and ν_S(P-(OH)$_2$) (magenta) modes: left - mean instantaneous frequencies from hybrid QM/MM trajectory; middle: harmonic (dashed) and anharmonic VCI (solid) frequencies of the $H_2PO_4^-\times 7H_2O$ cluster; right: local modes of the $H_2PO_4^-\times 7H_2O$ cluster. (c) Potential energy along normal modes Q_i in the $H_2PO_4^-\times 7H_2O$ cluster. (d) Molecular structure of $H_2PO_4^-$

fluctuations are modeled by an overdamped Brownian oscillator (OBO) model[41] parametrized by the QM/MM trajectory (for details see Sec. 5: Materials and Methods). We find good agreement of experiment and simulations for intensities, line shapes and frequency positions (with deviations typically below 10 cm^{-1}) for all $H_2PO_4^-$ stretching modes. Especially the broader, Voigt-like profiles of $\nu_{AS}(PO_2^-)$ and ν_{AS}(P-(OH)$_2$) compared to the more narrow, Lorentzian-shaped profile of $\nu_S(PO_2^-)$ are reproduced with excellent accuracy. The different line shapes are a direct consequence of the larger fluctuation bandwidth of $\nu_{AS}(PO_2^-)$ and ν_{AS}(P-(OH)$_2$) modes, highlighting the accuracy of the QM/MM Ansatz not only for averaged frequency positions but also the dynamics of solvent-induced ultrafast fluctuations. For the δ(P-(OH)$_2$) modes the intensity pattern is reproduced reasonably. We find that the v=0→1 transitions are significantly broadened compared to the $\nu_{AS}(PO_2^-)$ mode. However, a defined resonance can still be recognized while in the experiment the δ(P-(OH)$_2$) modes appear as an unstructured shoulder.

The Tavan group has simulated the linear absorption of phosphate ions, and in particular $H_2PO_4^-$ in solution[27,42]. Our instantaneous normal mode (INM) approach (Fig. 1a) is similar in spirit to the DFT/MM approach of Ref. 42. The decisive difference is that here two P-(OH) coordinated H_2O molecules are included in the QM region of INM which turned out to be crucial to accurately reproduce the frequency and intensity pattern of δ(P-(OH)$_2$) modes[28]. The Gaussian fluctuation profile of the QM:MM trajectory then allows to exploit the advantages of the OBO model for the efficient simulation of the linear absorption signal with reasonable accuracy. Compared to first-principles approach of Ref. 27 we report similar accuracy in frequency positions, intensities and line shapes of $\nu_{AS}(PO_2^-)$, $\nu_S(PO_2^-)$ and ν_{AS}(P-(OH)$_2$) modes with a somewhat better capability to reproduce the unstructured shoulder of δ(P-(OH)$_2$) modes. In Ref. 27 limited conformational statistics of the few tens of picoseconds trajectory were suggested to complicate an accurate simulation of the shoulder. The presented 2D signals (see Sec. 2.2.2) indicate that ultrafast dynamics dominate the line shapes.

2.2 2D IR spectra of $H_2PO_4^-$

Absorptive 2D spectra of the $H_2PO_4^-$ solution in a spectral range of 900–1300 cm^{-1} are shown in Fig. 2 for a waiting time T=0 fs. Peaks with yellow-red contours are caused by ground state bleaching (GSB) and/or stimulated emission (SE) of the v=0→1 transitions whereas peaks with blue contours arise from absorptions into the two-exciton manifold (excited state absorption (ESA) into overtone and combinations bands)[43]. The signals are dominated by peaks along the frequency diagonal (excitation frequency ν_1 = detection frequency ν_3) due to $\nu_S(PO_2^-)$ and $\nu_{AS}(PO_2^-)$ centered at ν_1=1080 and 1150 cm^{-1} as well as a weaker peak of ν_{AS}(P-(OH)$_2$) at ν_1=940 cm^{-1}. In contrast, the signal from δ(P-(OH)$_2$) has only minor v=0→1 contributions.

A striking feature of the $H_2PO_4^-$ 2D spectrum are the pronounced cross peaks between $\nu_S(PO_2^-)$ and $\nu_{AS}(PO_2^-)$ below and above the diagonal at (ν_1,ν_3)=(1080, 1150) cm^{-1} and (ν_1,ν_3)=(1150, 1080) cm^{-1}, respectively which suggest vibrational couplings between the PO_2^- stretching normal modes of the $H_2PO_4^-$ ion. While the lower cross peak (ν_1,ν_3)=(1080, 1150) cm^{-1} shows a tilt at T=0 fs, the upper cross peak (ν_1,ν_3)=(1150, 1080) cm^{-1} has a shoulder at low detection frequencies <1050 cm^{-1}.

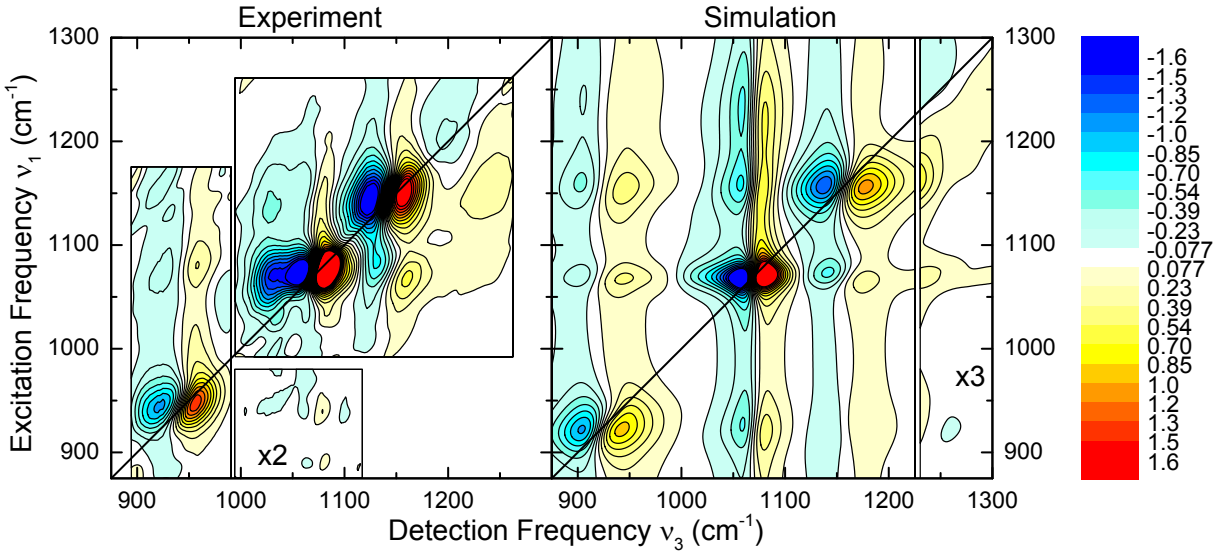

Fig. 2 Experimental (left) and simulated (right) 2D IR spectra of $H_2PO_4^-$ vibrations for a waiting time T=0 fs in the broad band frequency range 880–1300 cm^{-1}. The experimental broad band 2D IR signal has been constructed from three independent measurements as indicated by the boxes. The absorptive 2D signal is plotted as a function of excitation (ν_1) and detection (ν_3) frequency with an amplitude change of 10 % between neighboring contour lines. Yellow-red contours are due to v=0→1, blue contours due to v=1→2 transitions. The color scale illustrates the level of contour lines of 2D spectra in this article.

Cross peaks are also recognized between the PO_2^- and the P-$(OH)_2$ stretching modes, e.g. at (ν_1,ν_3)=(1080,950) cm^{-1}. Further weak cross peaks of PO_2^- stretching and the P-$(OH)_2$ bending modes arise at (ν_1,ν_3)=(1150,1240) cm^{-1} and (1080,1240) cm^{-1}. They appear as broad plateau close to the lowest contour corresponding to ≈10 % of the maximum signal.

In the following, we will explain how each of the experimental features in Fig. 2 (left) can be reproduced from a theoretical point of view (cf. Fig. 2, right) by providing a detailed account of the underlying physical mechanisms governing the 2D spectra. We start from an analysis of frequency fluctuations determining the diagonal-peak shapes in Sec. 2.2.1, followed by an analysis of the cross-peak positions and shapes containing information about vibrational couplings and Fermi resonances in Sec. 2.2.2 and 2.2.3. Cross-peak tilts and intensities arising from coherent quantum beats will be analyzed in Sec. 2.2.4.

2.2.1 Line shape analysis of ν_{AS}(P-(OH)$_2$) Diagonal peaks provide information about the line broadening mechanisms which have been analyzed in detail for $\nu_{AS}(PO_2^-)$ and $\nu_S(PO_2^-)$ using the frequency-fluctuation correlation function

$$C(t) = \langle \delta\nu(t)\delta\nu(0)\rangle \qquad (1)$$

as an input parameter for the simulation of the third-order nonlinear response[28]. $\delta\nu(t)$ is the time-dependent deviation from an average frequency and $\langle\ldots\rangle$ represents the ensemble average. The fairly round, upright peak shape indicative of a predominant homogeneous broadening has been attributed to ultrafast (< 100 fs) solvent-induced fluctuations supported by mixed quantum-classical INM analysis. Here we present additional data for ν_{AS}(P-$(OH)_2$) analyzing the dephasing in a Bloch picture.

Fig. 3 shows 2D spectra of ν_{AS}(P-$(OH)_2$) for waiting times T between 0 and 500 fs. The peaks are characterized by their nearly upright shape - similar to the PO_2^- stretching modes. The small tilt with respect to ν_1 is preserved within the observation window limited by the vibrational lifetime of ≈450 fs (pump-probe data are presented in Fig. S2, ESI†). That is, line shapes consist of a predominant homogeneous and a minor inhomogeneous contribution which allows to treat the vibrational dephasing in a Bloch picture. In this picture, the homogeneous component caused by fast frequency fluctuations is characterized by the pure dephasing time T_2^*, while the inhomogeneous frequency distribution $\Delta\nu_{inh}$ characterizes the static heterogeneity in the system. The pure dephasing time is determined by the fast frequency fluctuations through $T_2^* = ((2\cdot\pi\cdot c\cdot\Delta\nu_{hom})^2\cdot\tau_C)^{-1}$, where $\Delta\nu_{hom}$ and τ_C are the amplitudes and the characteristic correlation time of the underlying fluctuations. Using this approach we reduce the number of free parameters to calculate the 2D spectra compared to a biexponential Kubo function.

2D spectra are calculated within nonlinear response the-

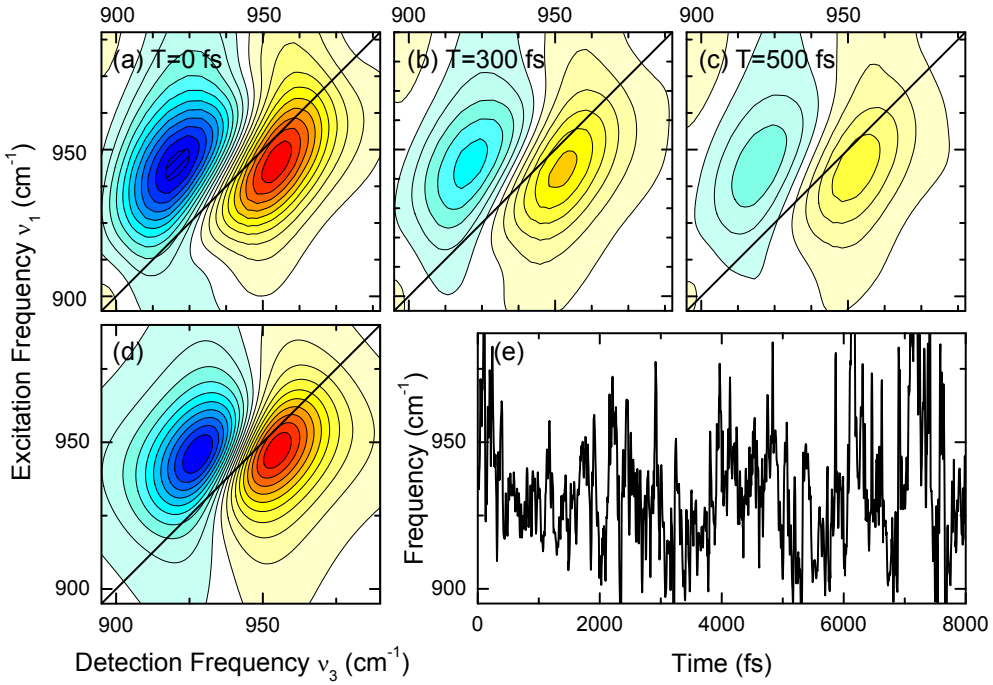

Fig. 3 2D IR spectra of ν_{AS}(P-(OH)$_2$) of $H_2PO_4^-$ in aqueous solution. (a-c): The experimental 2D spectra for waiting times T between 0 and 500 fs are plotted as a function of excitation (ν_1) and detection (ν_3) frequency with an amplitude change of 10 % between neighboring contour lines. The upright shape of all peaks in the spectra indicates a predominant homogeneous broadening due to fast frequency fluctuations. (d) Simulated 2D spectrum of ν_{AS}(P-(OH)$_2$) with a homogeneous dephasing time of T_2^*=700 fs indicating fast frequency modulations on a sub-100 fs timescale and a minor inhomogeneous frequency distribution of $\Delta\nu_{inh}$=10 cm^{-1}. (e) Time evolution of instantaneous frequencies of ν_{AS}(P-(OH)$_2$) in the mixed quantum-classical model. For color scale see Fig. 2.

ory. With the third order response functions outlined in the ESI†, we obtain the best fit to the experimental spectra with T_2^*=(700±100) fs and $\Delta\nu_{inh}$=(10±1) cm^{-1} (Fig. 3d). In the fast modulation limit, the inequality $\tau_C << T_2^*$ applies which supports previous findings of ultrafast frequency fluctuations of $H_2PO_4^-$ ions (τ_C <100 fs). Assuming a correlation time τ_C=50 fs found for librations in bulk water[13], we obtain a fluctuation amplitude of $\Delta\nu_{hom}$=28 cm^{-1}, matching the value derived for $\nu_{AS}(PO_2^-)$ in Ref. 28. Therefore, the results presented here provide additional proof that ultrafast librational motions of the $H_2PO_4^-$ hydration shell dominate the phosphate stretching line shapes.

In order to provide microscopic insight into the fastest frequency fluctuations revealed by line shape analysis of 2D spectra, we present the instantaneous frequency fluctuations of the ν_{AS}(P-(OH)$_2$) mode along the nuclear configurations generated by a classical MD trajectory. (for details see Ref. 28 and Sec. 5). A representative time evolution of frequencies within the first 8 ps is shown in Fig. 3e. The frequency-fluctuation correlation function (eq. 1) for ν_{AS}(P-(OH)$_2$) was calculated directly from the instantaneous frequencies of the trajectory. An exponential fit of the QM:MM derived correlation function yields an ultrafast component of τ_{C1}=50-75 fs in close agreement with the experiment. Similar agreement is obtained for the calculated mean frequency of ν_{AS}(P-(OH)$_2$) is 923 cm^{-1} and the fluctuation bandwidth $\sigma(\nu_{AS}$(P-(OH)$_2$)) = 27 cm^{-1} that is substantially larger than $\sigma(\nu_S(PO_2^-))$ = 16 cm^{-1} and similar to $\sigma(\nu_{AS}(PO_2^-))$ = 29 cm^{-1}.

2.2.2 Alignment of cross peaks: A global feature of the 2D spectra (Fig. 2) is the stripe-like pattern of stretching mode ($\nu_{AS}(PO_2^-)$, $\nu_S(PO_2^-)$, ν_S(P-(OH)$_2$)) cross peaks and diagonal peaks, i.e., their parallel alignment with respect to the excitation frequency axis ν_1. This pattern is caused by similar diagonal and off-diagonal anharmonicities of stretching modes which are significantly smaller than the linewidths. Theoretical anharmonicities on the order of 5–10 cm^{-1} are directly derived from VCI calculations (see Sec. 5.2.1, Eq. 5 for complete anharmonicity matrix), whereas a 'global' anharmonicity of ≈10 cm^{-1} is derived from 2D IR experiments taking the line shape and overlap effects into account. Note that only

2D spectroscopy allows for a direct test of the anharmonic potentials determined by the VCI calculations in Sec. 2.1. As such, the results in Fig. 2 map the potential energy surfaces from which we can derive <10 cm^{-1} coupling constants in the normal mode representation. In an alternative local mode picture of ν(P=O) and ν(P-(OH))phosphate stretching modes, additional bilinear inter-mode couplings of ≈ 40 cm^{-1} arise. The anharmonicities in the normal mode representation are substantially smaller compared to such bilinear coupling terms and the vibrational linewidths (20–50 cm^{-1}). Thus, they represent only a weak perturbation for two-exciton states (either combination bands or overtones) and the eigenvectors of two-exciton states can be identified as overtones/combination bands of the constituting one-exciton states. The good agreement of theoretical and experimental values leads to the similar stripe-like patterns in the 2D spectra (Fig. 2, right vs. left).

Additional cross peaks are found between the PO_2^- stretching and the δ(P-(OH)$_2$) bending modes at (ν_1,ν_3)=(1080,1250) and (1150,1250) cm^{-1}. However, in the simulation, they are too weak to be displayed by the lowest contour corresponding to 10 % of the maximum signal. If we artificially enhance the simulated signal we find qualitative agreement between experiment and theory where an unstructured ESA contribution arises near the diagonal together with a SE/GSB plateau indicative of cross peaks. In general δ(P-(OH)$_2$) cross peaks are more prominent than δ(P-(OH)$_2$) diagonal peaks in the 2D spectra. As the cross peak amplitudes in 2D spectra are weighted by the product of four successive transition dipole interactions, cross-peaks involving the strong $\nu_{S/AS}(PO_2^-)$ and the weak δ(P-(OH)$_2$) transitions appear more pronounced than δ(P-(OH)$_2$) diagonal peaks. Moreover the δ(P-(OH)$_2$) cross peaks appear broad and unstructured due to ultrafast fluctuations (fast modulation limit) and ultrashort sub-300 fs lifetime of δ(P-(OH)$_2$) modes. The unique information content of 2D spectra thus allows to reveal that the linear absorption line broadening mechanism (see high-frequency shoulder at 1250 cm^{-1} in Fig. 1) is due to short time dephasing dynamics rather than inhomogeneous broadening as suggested in Ref. 27.

2.2.3 Fermi-resonance coupling A striking feature in the experimental 2D spectra of $H_2PO_4^-$ is the plateau-like v=1→2 ESA (ν_1,ν_3)=(1075,1030) cm^{-1} which in the following will be microscopically assigned to a Fermi-resonance coupling mechanism of $\nu_S(PO_2^-)$ with a low-frequency tetrahedron skeleton mode (δ(O=P=O), harmonic frequency: 493 cm^{-1}; VCI: 506 cm^{-1}; see Tab.1). The assignment relies on high-level VCI calculations[37,38] performed for the $H_2PO_4^- \times 7H_2O$ cluster that expand the VCI wave function $|\mathbf{01}\rangle$ as linear combination

$$|\mathbf{01}\rangle = c_1|01\rangle \pm c_2|10\rangle ... \quad (2)$$

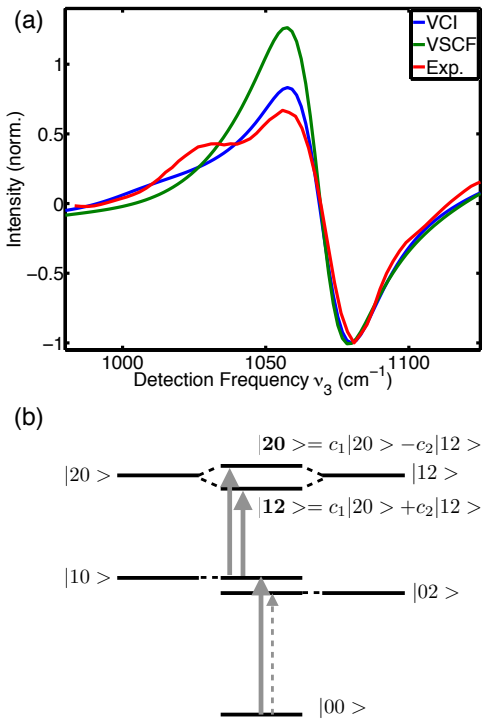

Fig. 4 (a) Cuts along the detection frequency ν_3 of simulated 2D IR spectra of $H_2PO_4^-$ (ν_1 = 1069 cm^{-1}): blue - full model including vibrational configuration interactions (VCI) between $\nu_S(PO_2^-)$ ($|a0\rangle$) and δ(O=P=O) modes ($|0b\rangle$); green - reduced model based on VSCF basis states; red - experimental cut (ν_1 = 1071 cm^{-1}); cuts have been normalized to v=0→1 GSB/SE contributions. (b) Schematic of mode mixing of $\nu_S(PO_2^-)$ ($|a0\rangle$) and δ(O=P=O) modes ($|0b\rangle$); solid arrows symbolize allowed transitions with strong dipole moments, dashed arrows symbolize negligible dipole moments. The respective expansion coefficients c_1 and c_2 are determined by the VCI method, for details see text.

in the basis of VSCF states (e.g. $|01\rangle$, $|10\rangle$, $|20\rangle$ ....)* and allow to access the correlated eigenvalues of single-exciton states (e.g. $|\mathbf{01}\rangle$), two-exciton states (combination $|\mathbf{02}\rangle$ and overtone $|\mathbf{11}\rangle$ bands, respectively) as well as the constituting expansion coefficients c_i. In the adopted $|ab\rangle$ notation, a and b represent quantum numbers of $\nu_S(PO_2^-)$ and δ(O=P=O), respectively.

We find that the δ(O=P=O) overtone $|\mathbf{02}\rangle$ is close in energy to the $|\mathbf{10}\rangle$ fundamental (1019 cm^{-1} and 1043 cm^{-1}, respectively on VCI level of theory, cf. Tab. 1) but both are almost pure states ($|\mathbf{10}\rangle = 0.97 \cdot |10\rangle + ...$; $|\mathbf{02}\rangle = 0.98 \cdot |02\rangle + ...$), in agreement with the linear absorption of $H_2PO_4^-$ where only the v=0→1 $\nu_S(PO_2^-)$ transition can be identified. As expected for overtones the dipole moment of the v=0→2 δ(O=P=O)

* we restrict our discussion to two modes indexed as $|ab\rangle$, the VCI/VSCF simulation in total account for the 15 $H_2PO_4^-$ modes; for details see Sec.5.2.1

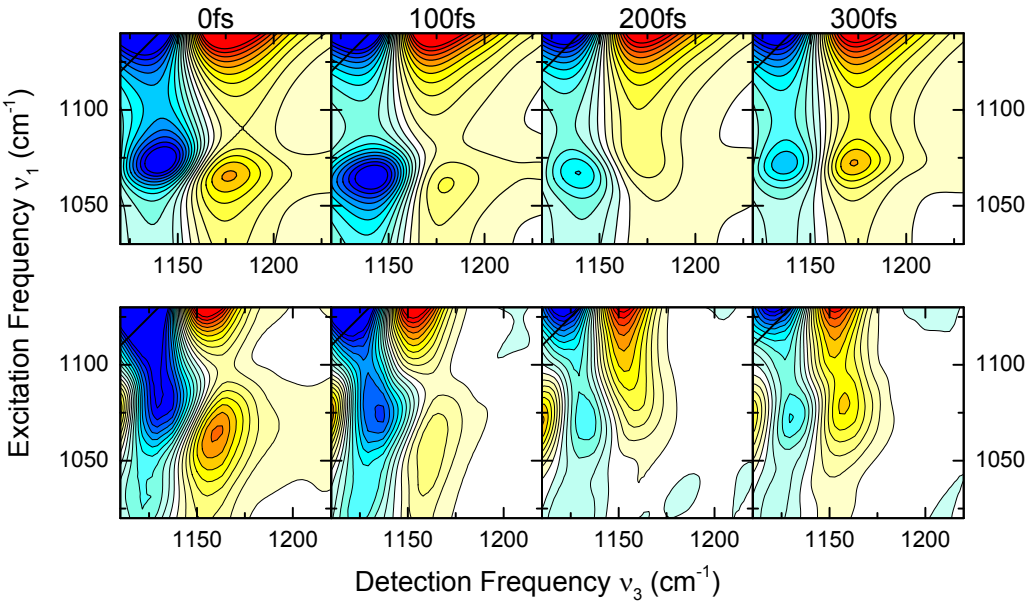

Fig. 5 Simulated (top) and experimental (bottom) 2D spectra of (ν_1,ν_3)= ($\nu_S(PO_2^-)$, $\nu_{AS}(PO_2^-)$) = (1080, 1150) cm^{-1} cross peak dynamics for waiting times T = 0, 100, 200 and 300 fs. The relative intensity of 2D IR spectra is normalized to the $\nu_{AS}(PO_2^-)$ diagonal peak. For color scale see Fig. 2.

transition is weak‡.

The situation changes for the ESA transition (ν_1,ν_3)=(1075,1030) cm^{-1}. The $|\mathbf{20}\rangle$ state is characterized by a strong mixing of $|20\rangle$ and $|12\rangle$ basis states

$$|\mathbf{20}\rangle = 0.86 \times |20\rangle + 0.43 \times |12\rangle ... \quad (3)$$

(and *vice versa* for $|\mathbf{12}\rangle$), where the two basis states account for a total weight of $\approx$ 93% in the correlated wave function. The weak perturbation limit is no longer applicable (Fig. 4b) and additionally the forbidden transition $|\mathbf{10}\rangle \rightarrow |\mathbf{12}\rangle$ acquires substantial transition strength. As a consequence, in the horizontal cuts of the simulation (ν_1=1069 cm^{-1}: blue line, Fig. 4a) the Fermi resonance coupling between $|20\rangle$ ($\nu_S(PO_2^-)$) and $|12\rangle$ (δ(O=P=O) overtone) induces a shoulder at ν_3 =1020 cm^{-1} caused by mode mixing and redistribution of transition strength within the bi-exciton manifold[44]. The line shape deviates from the Lorenzian-like line shape present in the absence of configuration mixing (cf. blue and green line, respectively). In contrast, the SE/GSB contribution arising from the v=0$\rightarrow$ 1 $\nu_S(PO_2^-)$ transition is unaffected. We observe qualitative agreement with experimental 2D spectra where an additional transition appears as pronounced shoulder along the ν_3 axis (red line, Fig. 4a). The experimental and theoretical determination of such features is challenging due to their broad band character.

The analysis of Fermi resonance coupling of the stretching mode $\nu_S(PO_2^-)$ with the low frequency tetrahedron skeleton mode δ(O=P=O) demonstrates that substantial mode mixing defines the wave functions within the bi-exciton manifold where the redistribution of transition strength makes the *per se* dark $|\mathbf{10}\rangle \rightarrow |\mathbf{12}\rangle$ overtone transition spectroscopically accessible. While in the single-exciton manifold the $|\mathbf{00}\rangle \rightarrow |\mathbf{02}\rangle$ overtone transition is dark due to the pure state characters, the VCI simulations demonstrate that the tetrahedron skeleton mode overtone is close in energy to the $\nu_S(PO_2^-)$ fundamental transition ($\Delta\nu(|\mathbf{10}\rangle - |\mathbf{02}\rangle)$ = 24 cm^{-1}) and that the energy splitting is comparable to the 15 cm^{-1} fluctuation bandwidth of $\nu_S(PO_2^-)$[28]. The anharmonicity of $\nu_S(PO_2^-)$ on the order of 5-10 cm^{-1} further reduces the splitting within the bi-exciton manifold, thus increasing the mode mixing of bi-excitons.

The PO_2^- stretching vibrations of $H_2PO_4^-$ in bulk H_2O possess lifetimes on the order of 300 fs[28] and the discussion above identifies low-frequency skeleton tetrahedron modes that serve as possible acceptors for vibrational energy. The respective Raman active O=P=O modes reported for A-and B-DNA[45] and double stranded RNA[46] posses vibrational frequencies of $\approx$ 500 cm^{-1} similar to $H_2PO_4^-$. Further theoretical investigations how the relevant inter-mode couplings and relative frequency positions determine the dissipation mechanism in the different systems are currently under investigation. Additional experiments using terahertz pulses will open a route to directly probe the relaxation pathways. Here phosphate ions

‡ $\mu^2_{\nu_S(PO_2^-)}/\mu^2_{\delta(O=P=O)}$ = 57. The weak v=0$\rightarrow$2 δ(O=P=O) transition moment arises predominantly from configuration interactions while mode anharmonicities are minor ($^{VCI}\mu^2_{\delta(O=P=O)}/^{VSCF}\mu^2_{\delta(O=P=O)} = 119$).

serve as small, tractable model systems for energy dissipation of phosphate groups in biomolecules such as DNA and phospholipids[29,30,47,48]. The understanding of such phenomena is the key to microscopic insight into DNA damage or chemistry at cell membrane interfaces.

2.2.4 Cross-peak dynamics In Fig. 5 we compare the simulated (top row) and experimental (bottom row) dynamics of the stretching modes cross peak (ν_1,ν_3) =($\nu_S(PO_2^-)$, $\nu_{AS}(PO_2^-)$) = (1080, 1150) cm^{-1} for waiting times T=0, 100, 200 and 300 fs. The negative cross peak (blue contours) is caused by the ESA from the v=1 state of $\nu_S(PO_2^-)$ into the combination band of $\nu_S(PO_2^-)$ and $\nu_{AS}(PO_2^-)$, whereas the positive cross peak (yellow-red contours) is due to the GSB and SE from of the v=1 state of $\nu_{AS}(PO_2^-)$ (cf. double-sided ladder diagrams in Fig. 6c).

Starting at a waiting time T=0 fs, a tilt of the cross peaks relative to the ν_1 axis can be identified. This behavior is most obvious by observing the shape of the zero contour (white). The tilt appears more pronounced than the static tilt of diagonal peaks caused by inhomogeneous contribution to the signal (cf. Fig. 2), and shows a dynamic behavior: for T=100 fs the tilt relative to the ν_1 axis is diminished, slightly reversed for T=200 fs and for T=300 fs upright cross peaks are observed.

Further dynamics manifests in the time evolution of relative amplitudes of the GSB/SE and ESA contributions. We observe a relative decrease of GSB/SE contribution from T=0–100 fs, followed by a decrease of the ESA contribution until T=200 fs and a further increase of the GSB/SE contribution until T=300 fs, suggesting an oscillatory behavior present in cross peak dynamics during T evolution. We point out that theory and experiment show a very nice agreement for both of the above mentioned features, i.e., the T-dependent tilt of the cross peaks as well as the amplitude modulations.

We performed additional simulations on a reduced model, which takes into account energy levels of $\nu_{AS}(PO_2^-)$ and $\nu_S(PO_2^-)$ stretching modes together with the dark Fermi-resonance mode (cf. Sec. 2.2.3), neglecting contributions of bending modes (δ_{AS}(P-(OH)$_2$), δ_S(P-(OH)$_2$)) and the ν_{AS}(P-(OH)$_2$) stretching mode (respective simulated 2D signals are given in Fig. S5, ESI†). The reduced model is designed to closely resemble the experimental excitation conditions which due to the limited spectral bandwidth of pulses (200 cm^{-1}) coherently excite $\nu_{AS}(PO_2^-)$ and $\nu_S(PO_2^-)$ stretching modes only. The T dependence of cross-peak intensity relative to the mean is shown in Fig. 6a. Both cross-peak intensities (ESA and SE, blue and green line, respectively) oscillate in an anti-correlated manner. Their coherent evolution shows an oscillation with a period of about 360 fs. Moreover the dynamic cross-peak tilt is qualitatively reproduced in the coherent two-mode model (Fig. S5, ESI†, see below for discussion). As the model accounts for single-exciton lifetimes (phenomenological single-exciton to ground state transport rates $1/k_{i0} = 300$ fs) but neglects incoherent intermode transport (for details see Sec. 5 and ESI†) the T dependence of cross-peak intensity solely arises from the coherent evolution of the wavepacket generated in $\nu_{AS}(PO_2^-)$ and $\nu_S(PO_2^-)$ stretching modes. Respective Fourier transforms of cross-peak beatings are presented in Fig. 6b and reveal a frequency of 80–90 cm^{-1} corresponding to the difference frequency of $\nu_{AS}(PO_2^-)$ and $\nu_S(PO_2^-)$ (89 cm^{-1}, cf. Table 1). The width is a direct consequence of the sub-ps dephasing of the $\nu_{AS}(PO_2^-)$ / $\nu_S(PO_2^-)$ quantum beat.

In the experiment (Fig. 6a, red symbols) we observe a beating of the cross-peak intensity at the position of the SE cross-peak that closely resembles the oscillation period of the simulation (the coherent beating of the ESA cross peak is scrambled due to overlap with the diagonal peak). Further support for the interpretation of a PO_2^- stretching-mode quantum beat comes from pump-probe data (Fig. S3, ESI†). Analysis of the transients reveals a weak coherent oscillation on top of the transient decay with a frequency of $\approx$ 90 cm^{-1} in consistence with the calculations. However, only 2D spectra allow for an assignment of the origin of coherent beating from diagonal or cross peaks.

As we perform photon-echo experiments in the boxcar geometry, rephasing and non-rephasing contributions are readily disentangled. It was demonstrated that oscillations of cross peaks arise from the rephasing contribution to 2D signal[49,50]. The relevant Liouville space pathways of coherent quantum beats during T can be analyzed in a diagrammatic approach ($k_R = -k_{\omega_S} + k_{\omega_{AS}} + k_{\omega_S}$, relevant double sided ladder diagrams are given in Fig. 6c). A $|01\rangle\langle 10|$ coherence of two coupled anharmonic oscillators during waiting time T can be observed as coherent beating of cross peaks at the frequency positions (ν_1, ν_3) =($\nu_S(PO_2^-)$, $\nu_{AS}(PO_2^-)$) and ($\nu_S(PO_2^-)$, $\nu_{AS}(PO_2^-)$ - $\Delta_{S,AS}$), where $\Delta_{S,AS}$ denotes the anharmonicity of the combination band (Fig. 6c, top row). The population diagrams (Fig. 6c, bottom row) together with the non-rephasing counterparts induce a non-oscillating background at respective frequency positions. The coherent part $R^{(c)}(t_3,t_2,t_1)$ of the response function (cf. ESI†) is responsible for the observed quantum beats in the simulated 2D signals. Incoherent intermode transport typically occurs on the low ps timescale[29,51], outside the current observation window. Moreover within the employed secular approximation that decouples populations and coherences, incoherent intermode transport only affects the non-oscillating background.

A qualitative confirmation is obtained by a decomposition of the experimental absorptive 2D signal into rephasing and non-rephasing contributions (Fig. S4, ESI†). The rephasing 2D signal exhibits a coherent beating of the cross-peak intensity similar to the absorptive signal while the cross-peak intensity in the non-rephasing signal is constant within the experimental accuracy. This behavior also allows for an explanation

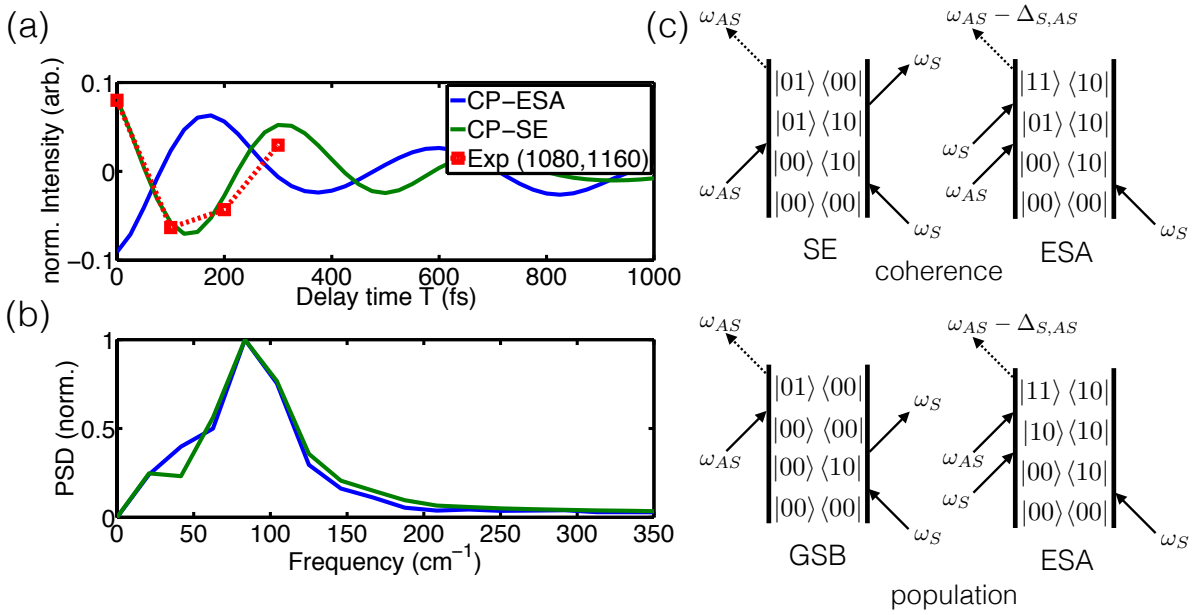

Fig. 6 (a) Cross-peak intensity normalized to the decay of $\nu_S(PO_2^-)$ in 2D IR spectra of $H_2PO_4^-$ for waiting times T = 0–1000 fs: blue line - simulated ESA cross peak ($|01\rangle \rightarrow |11\rangle$), green line - simulated SE cross peak , red symbols - experimental SE cross peak. Simulations are performed for a reduced model consisting of $\nu_{AS}(PO_2^-)$ and $\nu_S(PO_2^-)$ stretching modes and the dark Fermi-resonance mode, for details see text. (b) normalized power spectrum of the Fourier transform of the oscillatory signal. (c) relevant double sided ladder diagrams: top-coherent rephasing pathways responsible for quantum beats ($|01\rangle\langle 10|$) of the cross-peak during waiting time T; bottom - population rephasing diagrams (e.g. $|10\rangle\langle 10|$) responsible for incoherent background at the cross-peak position. Interchange of the first two pulses allows for respective non-rephasing population diagrams. $|10\rangle$ denotes the v=1 state of $\nu_S(PO_2^-)$, $|01\rangle$ denotes the v=1 state of $\nu_{AS}(PO_2^-)$ and $|11\rangle$ denotes the two-exciton combination band of $\nu_S(PO_2^-)$ and $\nu_{AS}(PO_2^-)$; for details see text.

of the dynamic cross-peak tilt. At T=0 fs the rephasing contribution dominates, leading to a tilt of the cross peaks parallel to the diagonal. The opposite cross-peak tilt at T=200 fs is the fingerprint of the non-rephasing contribution whose amplitude is non-oscillating and the relative contribution to the absorptive 2D signal is maximal at this T.

We note that oscillatory features in time-resolved vibrational spectroscopy can arise from broad-band excitations of either a quantum beat of coupled modes within the pulse spectrum[49,51–56] or a wave packet of low-frequency modes in an impulsive Raman process[57,58]. The presented analysis of 2D spectra in terms of rephasing and non-rephasing contributions allows to safely assign the origin on the basis of the contributing Liouville space pathways and reveals coherent beating at unique frequency positions of cross peaks that only arise due to quantum beats of the coupled $\nu_S(PO_2^-)$ and $\nu_{AS}(PO_2^-)$ modes.

3 Conclusions

Reported examples of vibrational coherent quantum beats directly observed in 2D spectra benefit from the longer vibrational lifetimes in nonaqueous solution[49,51,53,54,56]. Here we conclusively demonstrated for the first time that the low frequency phosphate modes of $H_2PO_4^-$ ions show long lived coherent vibrational motion on the order of hundreds of femtoseconds in aqueous solution, that is substantially longer than the sub-100 fs correlation time of frequency fluctuations of PO_2^- and $P(OH)_2$ stretching modes imposed by ultrafast librational fluctuations of the solvent. Due to the small splitting of $\nu_S(PO_2^-)$ and $\nu_{AS}(PO_2^-)$ modes the $H_2PO_4^-$ ion appears an ideal model system to study the coherent evolution and associated dephasing mechanisms in solution.

The unique information content of third-order spectroscopy is exploited by photon-echo experiments combined with ab-initio based modeling to provide a complete characterization of $H_2PO_4^-$ phosphate stretching vibrations and the interactions with its hydration shell. Hereby we comprehensively unravel the character of sub-100 fs frequency fluctuations as well as 5–10 cm^{-1} intramolecular couplings and anharmonicities in a natural water environment. Tetrathedron skeleton modes are identified as possible acceptor modes for ultrafast energy dissipation of phosphate stretching vibrations. Microscopic modeling together with ultrafast spectroscopy at even lower fre-

quencies might be an exciting avenue for future research in order to boost the understanding of ultrafast energy dissipation in phosphate ions and ultimately biomolecules like DNA and phospholipids.

4 Acknowledgement

We thank Thomas Elsaesser for continuous support and valuable discussions. The research leading to these results has received funding from the European Research Council under the European Union's Seventh Framework Programme (FP7/2007-2013)/ERC Grant. Agreement No. 247051. B.P.F. gratefully acknowledges support through the German Research Foundation (DFG) within the Emmy Noether Programme (Grant No. FI 2034/1-1).

5 Materials and Methods

5.1 Experiment

The experimental setup and the experimental conditions are the same as described in Ref. 28. Briefly, 100 fs mid-IR pulses in the spectral range between 900 and 1200 cm^{-1} were generated in home-built frequency converters[59] pumped by an amplified Ti:sapphire laser system (Coherent Legent Elite). Third-order nonlinear signals of a photon-echo experiment in the boxcar geometry were measured as a function of coherence time τ (time delay between the first two pulses) and waiting time T (time delay between the second and third pulse) by heterodyne detection with a weak local oscillator pulse. The excitation frequency axis ν_1 of 2D spectra for fixed T is obtained by a Fourier transform of the nonlinear signal with respect to τ, whereas the detection frequency axis ν_3 is obtained by spectrally resolved detection with a monochromator and a 64-pixel HgCdTe detector array.

For the time-resolved experiments, a 1 M solution of KH_2PO_4 in H_2O was held as a 10 μm thick wire-guided liquid jet[60] in order to avoid nonresonant interaction of the pulses with sample windows. For the deuteration experiments, 1 M KH_2PO_4 was dissolved in D_2O leading to a negligible H/D ratio of $<2\%$. Linear absorption spectra were measured in attenuated total reflectance (ATR) mode (Pike MIRacle, Varian 640-IR).

5.2 Theoretical Modeling

5.2.1 Model Hamiltonian The simulation of linear absorption and 2D-IR spectra is based on model Hamiltonian parametrization that combines hybrid-quantum classical simulations for fundamental transition, and frequency fluctuations with ab-initio *VCI/VSCF* results on $H_2PO_4^- \times 7\ H_2O$ cluster for anharmonicies and inter mode couplings.

Hybrid quantum-classical simulation protocol: Instantaneous frequencies of $H_2PO_4^-$ where calculated along successive configurations of a classical MD trajectory[61–64] as detailed in Ref. 28. The solute $H_2PO_4^-$ and two P-OH coordinated H_2O molecules are treated on hybrid DF(B3LYP) level of theory (Basis: 6-311++G(d,p))[65] in the field of point charges of all remaining water molecules. Relaxed instantaneous normal modes (rINM) are evaluated by initially optimizing the $H_2PO_4^- \times 2H_2O$ QM region and subsequent normal mode analysis.

VCI/VSCF method. The microsolvated clusters $H_2PO_4^- \times xH_2O$ ($x = 5/7$) are generated by successively adding a water molecule followed by geometry optimization, and confirmed by harmonic normal mode analysis. The *VCI/VSCF* method then allows to investigate anharmonicities and mode couplings beyond the harmonic approximation in a two step procedure: in brief, inter-mode couplings are considered by restricting the many-body expansion of the potential energy surface (PES) to 2D potential terms $V(Q_i, Q_j)$ (where $Q_{i,j}$ denote vibrational degrees of freedom). It has been shown that the $V(Q_i, Q_j)$ terms provide sufficient accuracy in complex molecular systems with many degrees of freedom[66]. Vibrational fundamental and bi-exciton (overtone and combination) transitions are obtained in a vibrational self-consistent field (*VSCF*) calculation. The VSCF states (e.g. $|01\rangle$, $|10\rangle$, $|20\rangle$ ....) then serve as basis states for a vibrational configuration interaction treatment (VCI) where the VCI wave function is expanded as a linear combination of the form $|\mathbf{01}\rangle = c_1|01\rangle \pm c_2|10\rangle ...$ (where bold type denotes CI states) and the expansions coefficients c_i are to be determined. The VCI treatment accounts for correlation effects of vibrational states beyond the VSCF mean field approach. All vibrational modes of the solute $H_2PO_4^-$ (15 modes) are included in the VCI/VSCF simulations[34–39]. (cf. Sec. 2.2.3 and Table 1, IR frequencies of the $H_2PO_4^- \times 5\ H_2O$ cluster are given in the ESI†).

Fundamental Transitions and Anharmonicities. The employed parametrization relies on the normal mode representation and starts with the system Hamiltonian[67]

$$\hat{H}_0 = \hbar \sum_i \varepsilon_i \hat{B}_i^\dagger \hat{B}_i + \hbar \sum_{ij,kl} U_{ij,kl} \hat{B}_i^\dagger \hat{B}_j^\dagger \hat{B}_k \hat{B}_l. \qquad (4)$$

For the the single exciton manifold (fundamental transition) bilinear couplings are absent in the normal mode representation. We consider the fundamental transitions of δ_{AS}(P-(OH)$_2$), δ_S(P-(OH)$_2$) , ν_{AS}(PO_2^-), ν_S(PO_2^-) and ν_{AS}(P-(OH)$_2$) augmented by the overtone transition of δ(O=P=O) (labeled as modes $\nu_{1,2...6}$ respectively) which are characterized by unscaled mean instantaneous frequencies obtained from the hybrid QM/MM trajectory (Table 1). For the bi-exciton manifold we consider all 21 possible combinations of single-excitons

(combination bands and overtones) which are defined by the quartic couplings $U_{ij,kl}$. The diagonal terms $U_{ii,ii} = A_{ii}$ denote anharmonicities while off-diagonal terms $U_{ii,jj} = A_{ij}$ denote intermode couplings. A_{ij} are derived from VCI/VSCF calculations on the $H_2PO_4^- \times 7H_2O$ cluster (in cm^{-1}):

$$A_{i,j} = \begin{pmatrix} 8.5 & & & & \\ -7.4 & 26.5 & & & \\ 3.5 & -3.1 & 10.9 & & \\ 0.0 & -0.1 & 4.0 & 5.0 & \\ -0.4 & 1.3 & 2.3 & 0.4 & 3.0 \end{pmatrix} \quad (5)$$

Fermi resonance coupling is accounted for by the tetradic anharmonicity matrix $U_{ij,kl}$ (i.e. the single matrix element between $\nu_S(PO_2^-)$ overtone and the $\nu_S(PO_2^-)$ - δ(O=P=O) combination band $U_{44,64}$ = 25.5 cm^{-1}). The Fermi resonance coupling strength $U_{44,64}$ is adjusted that the eigenvectors of a reduced bi-exciton two state Hamiltonian of $\nu_{AS}(PO_2^-)$ and δ(O=P=O) modes reproduces the mixing of VSCF/VCI states ($|\mathbf{20}\rangle = 0.86 \times |20\rangle + 0.43 \times |12\rangle$, cf. Sec. 2.2.3)

Dipole moments are taken along the direction of the harmonic mode dipole moment vectors and rescaled according to the VSC/VCI values (Table 1).

5.2.2 Overdamped-Brownian Oscillator (OBO) Model: The Gaussian fluctuation profile of instantaneous frequencies[28] justifies the use of a OBO model where the spectral density is given by

$$\tilde{C''}(\omega) = 2\lambda \frac{\omega\Lambda}{\omega^2 + \Lambda^2} \quad (6)$$

and defined by the bath timescale Λ and the system-bath coupling strength λ. The parameters of the OBO model in the high temperature limit are adopted to the frequency-frequency fluctuation correlation function directly calculated from the fluctuations of instantaneous frequencies of the hybrid QM/MM trajectory (Λ = 50 fs)[28](see ESI†). A static inhomogeous contribution is used for generation random single-exciton Hamiltonians centered around ω_i with Gaussian width $\delta\nu_{i,static}$. Correlations of fluctuations between modes are characterized by the cross-correlation coefficients of the frequency-frequency fluctuation correlation function

$$C_{ij} = \frac{1}{\sqrt{\Delta\nu_i^2 \Delta\nu_j^2}} \langle (\nu_i - \overline{\nu}_i)(\nu_j - \overline{\nu}_j) \rangle \quad (7)$$
$$= \begin{pmatrix} 1 & & & & \\ 0.04 & 1 & & & \\ 0.31 & 0.42 & 1 & & \\ 0.37 & 0.18 & 0.47 & 1 & \\ 0.16 & 0.40 & 0.21 & 0.22 & 1 \end{pmatrix}$$

where $\langle ... \rangle$ denotes averaging over the trajectory and $\overline{\nu}_{i/j}$ the average frequency of mode i, j, respectively. C_{ij} are related to the sytem-bath coupling matrix λ_{ij} given as (in cm^{-1}):

$$\lambda_{i,j} = \begin{pmatrix} 4.6 & & & & \\ 0.2 & 4.4 & & & \\ 0.9 & 1.2 & 1.8 & & \\ 0.6 & 0.3 & 0.5 & 0.6 & \\ 0.4 & 1.0 & 0.4 & 0.2 & 1.6 \end{pmatrix} \quad (8)$$

We find the strongest correlation for $\nu_{AS}(PO_2^-)$ and $\nu_S(PO_2^-)$ ($C_{34} = 0.47$) and correlated fluctuations of substantial strength between $\nu_{AS}(PO_2^-)$ and δ(P-(OH)$_2$ ($C_{23} = 0.42$). Test simulations show that a model with correlated fluctuations of single-exciton states is able to reproduce the dynamical behavior of cross-peak tilting in slightly better agreement than a uncorrelated model, especially for the tilting of cross peaks for $T > 0$ fs.

5.2.3 Signal Simulations: Linear absorption and 2D IR signals are simulated in the sum-over-states approach with the response function evaluated by the cumulant expansion[41,68] and the high temperature OBO lineshape function detailed in the ESI†. We employ the Doorway-Window factorization[67,69] that accounts for incoherent transport (secular approximation) and use phenomenological single-exciton to ground state transport rates only ($1/k_{i0} = 300$ fs) to account for the experimentally observed lifetimes of vibrational modes, while intermode transport is neglected. Incoherent intermode transport typically occurs on the low ps timescale[29,51], outside the current observation window. The full response function is given in the ESI†. Inhomogenous broadening is accounted for by averaging the 2D absorptive spectra over 50 realizations.

References

1 B. Alberts, A. Johnson, J. Lewis, M. Raff, K. Roberts and P. Walter, *Molecular biology of the cell*, Garland Science, Taylor & Francis Group, 5th edn, 2008.
2 F. Westheimer, *Science*, 1987, **235**, 1173–1178.
3 M. Pasenkiewicz-Gierula, Y. Takaoka, H. Miyagawa, K. Kitamura and A. Kusumi, *J. Phys. Chem. A*, 1997, **101**, 3677–3691.
4 B. Schneider, K. Patel and H. M. Berman, *Biophys. J.*, 1998, **75**, 2422 – 2434.
5 N. M. Levinson, E. E. Bolte, C. S. Miller, S. A. Corcelli and S. G. Boxer, *J. Am. Chem. Soc.*, 2011, **133**, 13236–13239.
6 F. Xia, T. Rudack, Q. Cui, C. Kötting and K. Gerwert, *J. Am. Chem. Soc.*, 2012, **134**, 20041–20044.
7 R. P. B, N. V. Plotnikov, J. Lameira and A. Warshel, *Proc. Natl. Acad. Sci. U. S. A.*, 2013, **110**, 20509–20514.
8 J. D. Watson and F. H. C. Crick, *Nature*, 1953, **171**, 737–738.
9 W. Saenger, W. N. Hunter and O. Kennard, *Nature*, 1986, **324**, 385–388.
10 H. M. Berman, J. Westbrook, Z. Feng, G. Gilliland, T. N. Bhat, H. Weissig, I. N. Shindyalov and P. E. Bourne, *Nucleic Acids Res.*, 2000, **28**, 235–242.
11 S. Pasqualato and J. Cherfils, *Structure*, 2005, **13**, 533–540.
12 J. B. Asbury, T. Steinel, K. Kwak, S. A. Corcelli, C. P. Lawrence, J. L. Skinner and M. D. Fayer, *J. Chem. Phys*, 2004, **121**, 12431–12446.

13 M. L. Cowan, B. D. Bruner, N. Huse, J. R. Dwyer, B. Chugh, E. T. J. Nibbering, T. Elsaesser and R. J. D. Miller, *Nature*, 2005, **434**, 199–202.

14 J. Savolainen, S. Ahmed and P. Hamm, *Proc. Natl. Acad. Sci. U. S. A.*, 2013, **110**, 20402–20407.

15 A. T. Krummel, P. Mukherjee and M. T. Zanni, *J. Phys. Chem. B*, 2003, **107**, 9165–9169.

16 M. Yang, Ł. Szyc and T. Elsaesser, *J. Phys. Chem. B*, 2011, **115**, 1262–1267.

17 S. Pal, P. K. Maiti, B. Bagchi and J. T. Hynes, *J. Phys. Chem. B*, 2006, **110**, 26396–26402.

18 Y. S. Kim and R. M. Hochstrasser, *J. Phys. Chem. B*, 2009, **113**, 8231–8251.

19 Z. Ganim, H. S. Chung, A. W. Smith, L. P. DeFlores, K. C. Jones and A. Tokmakoff, *Acc. Chem. Res.*, 2008, **41**, 432–441.

20 J. T. King and K. J. Kubarych, *J. Am. Chem. Soc.*, 2012, **134**, 18705–18712.

21 A. C. Fogarty, E. Duboue-Dijon, F. Sterpone, J. T. Hynes and D. Laage, *Chem. Soc. Rev.*, 2013, **42**, 5672–5683.

22 M. Ji, M. Odelius and K. J. Gaffney, *Science*, 2010, **328**, 1003–1005.

23 J. Borek, F. Perakis, F. Kläsi, S. Garrett-Roe and P. Hamm, *J. Chem. Phys.*, 2012, **136**, 224503.

24 D. Laage and J. T. Hynes, *Proc. Natl. Acad. Sci. U. S. A.*, 2007, **104**, 11167–11172.

25 A. B. Pribil, T. S. Hofer, B. R. Randolf and B. M. Rode, *J. Comput. Chem.*, 2008, **29**, 2330–2334.

26 E. Tang, D. Di Tommaso and N. H. de Leeuw, *J. Chem. Phys*, 2009, **130**, 234502.

27 J. VandeVondele, P. Tröster, P. Tavan and G. Mathias, *J. Phys. Chem. A*, 2012, **116**, 2466–2474.

28 R. Costard, T. Tyborski, B. P. Fingerhut and T. Elsaesser, *J. Chem. Phys.*, 2015, **142**, 212406.

29 T. Siebert, B. Guchhait, Y. Liu, R. Costard and T. Elsaesser, *J. Phys. Chem. B*, 2015, **119**, 9670–9677.

30 R. Costard, I. A. Heisler and T. Elsaesser, *J. Phys. Chem. Lett.*, 2014, **5**, 506–511.

31 S.-T. Sun, L. Jiang, J. Liu, N. Heine, T. I. Yacovitch, T. Wende, K. R. Asmis, D. M. Neumark and Z.-F. Liu, *Phys. Chem. Chem. Phys.*, 2015, **doi: 10.1039/C5CP02253C**, –.

32 J. A. Boatz and M. S. Gordon, *J. Phys. Chem.*, 1989, **93**, 1819–1826.

33 M. W. Schmidt, K. K. Baldridge, J. A. Boatz, S. T. Elbert, M. S. Gordon, J. H. Jensen, S. Koseki, N. Matsunaga, K. A. Nguyen, S. Su, T. L. Windus, M. Dupuis and J. A. Montgomery, *J. Comput. Chem.*, 1993, **14**, 1347–1363.

34 G. Rauhut, *J. Chem. Phys.*, 2004, **121**, 9313–9322.

35 T. Hrenar, H.-J. Werner and G. Rauhut, *J. Chem. Phys*, 2007, **126**, 134108.

36 G. Rauhut and T. Hrenar, *Chem. Phys.*, 2008, **346**, 160 – 166.

37 M. Neff and G. Rauhut, *J. Chem. Phys.*, 2009, **131**, 124129.

38 M. Neff, T. Hrenar, D. Oschetzki and G. Rauhut, *J. Chem. Phys.*, 2011, **134**, 064105.

39 H.-J. Werner, P. J. Knowles, G. Knizia, F. R. Manby, M. Schütz, P. Celani, T. Korona, R. Lindh, A. Mitrushenkov, G. Rauhut, K. R. Shamasundar, T. B. Adler, R. D. Amos, A. Bernhardsson, A. Berning, D. L. Cooper, M. J. O. Deegan, A. J. Dobbyn, F. Eckert, E. Goll, C. Hampel, A. Hesselmann, G. Hetzer, T. Hrenar, G. Jansen, C. Köppl, Y. Liu, A. W. Lloyd, R. A. Mata, A. J. May, S. J. McNicholas, W. Meyer, M. E. Mura, A. Nicklass, D. P. O'Neill, P. Palmieri, D. Peng, K. Pflüger, R. Pitzer, M. Reiher, T. Shiozaki, H. Stoll, A. J. Stone, R. Tarroni, T. Thorsteinsson and M. Wang, *MOLPRO, version 2012.1, a package of ab initio programs*.

40 S. A. Corcelli, C. P. Lawrence and J. L. Skinner, *J. Chem. Phys.*, 2004, **120**, 8107–8117.

41 S. Mukamel, *Principles of Nonlinear Optical Spectroscopy (Oxford Series on Optical and Imaging Sciences)*, Oxford University Press, USA, 3rd edn, 1999.

42 M. Klähn, G. Mathias, C. Kötting, M. Nonella, J. Schlitter, K. Gerwert and P. Tavan, *J. Phys. Chem. A*, 2004, **108**, 6186–6194.

43 P. Hamm and M. Zanni, *Concepts and Methods of 2D Infrared Spectroscopy*, Cambridge University Press, 1st edn, 2011.

44 T. Brinzer, E. J. Berquist, Z. Ren, S. Dutta, C. A. Johnson, C. S. Krisher, D. S. Lambrecht and S. Garrett-Roe, *J. Chem. Phys.*, 2015, **142**, 212425.

45 G. J. Thomas Jr., J. M. Benevides, S. A. Overman, T. Ueda, K. Ushizawa, M. Saitoh and M. Tsuboi, *Biophys. J.*, 1995, **68**, 1073 – 1088.

46 J. M. Benevides, M. Tsuboi, J. K. Bamford and G. J. Thomas Jr., *Biophys. J.*, 1997, **72**, 2748 – 2762.

47 Ł. Szyc, M. Yang and T. Elsaesser, *J. Phys. Chem. B*, 2010, **114**, 7951–7957.

48 N. E. Levinger, R. Costard, E. T. J. Nibbering and T. Elsaesser, *J. Phys. Chem. A*, 2011, **115**, 11952–11959.

49 M. Khalil, N. Demirdöven and A. Tokmakoff, *J. Chem. Phys.*, 2004, **121**, 362–373.

50 Y.-C. Cheng and G. R. Fleming, *J. Phys. Chem. A*, 2008, **112**, 4254–4260.

51 D. B. Wong, C. H. Giammanco, E. E. Fenn and M. D. Fayer, *J. Phys. Chem. B*, 2013, **117**, 623–635.

52 D. Cringus, T. l. C. Jansen, M. S. Pshenichnikov and D. A. Wiersma, *J. Chem. Phys.*, 2007, **127**, 084507.

53 T. l. C. Jansen, D. Cringus and M. S. Pshenichnikov, *J. Phys. Chem. A*, 2009, **113**, 6260–6265.

54 M. J. Nee, C. R. Baiz, J. M. Anna, R. McCanne and K. J. Kubarych, *J. Chem. Phys.*, 2008, **129**, 084503.

55 C. Greve, N. K. Preketes, R. Costard, B. Koeppe, H. Fidder, E. T. J. Nibbering, F. Temps, S. Mukamel and T. Elsaesser, *J. Phys. Chem. A*, 2012, **116**, 7636–7644.

56 L. Chuntonov and J. Ma, *J. Phys. Chem. B*, 2013, **117**, 13631–13638.

57 K. Heyne, N. Huse, J. Dreyer, E. T. J. Nibbering, T. Elsaesser and S. Mukamel, *J. Chem. Phys.*, 2004, **121**, 902–913.

58 M. Banno, K. Ohta and K. Tominaga, *Phys. Chem. Chem. Phys.*, 2012, **14**, 6359–6366.

59 R. A. Kaindl, M. Wurm, K. Reimann, P. Hamm, A. M. Weiner and M. Woerner, *J. Opt. Soc. Am. B*, 2000, **17**, 2086–2094.

60 M. J. Tauber, R. A. Mathies, X. Chen and S. E. Bradforth, *Rev. Sci. Instrum.*, 2003, **74**, 4958–4960.

61 D. van der Spoel, E. Lindahl, B. Hess, G. Groenhof, A. E. Mark and H. J. Berendsen, *J. Comput. Chem.*, 2005, **26**, 1701–1718.

62 B. Hess, C. Kutzner, D. van der Spoel and E. Lindahl, *J. Chem. Theory. Comput.*, 2008, **4**, 435–447.

63 A. D. MacKerell Jr., N. Banavali and N. Foloppe, *Biopolymers*, 2001, **56**, 257–265.

64 M. W. Mahoney and W. L. Jorgensen, *J. Chem. Phys.*, 2000, **112**, 8910–8922.

65 M. Valiev, E. Bylaska, N. Govind, K. Kowalski, T. Straatsma, H. V. Dam, D. Wang, J. Nieplocha, E. Apra, T. Windus and W. de Jong, *Comput. Phys. Commun.*, 2010, **181**, 1477 – 1489.

66 T. K. Roy and R. B. Gerber, *Phys. Chem. Chem. Phys.*, 2013, **15**, 9468–9492.

67 D. Abramavicius, B. Palmieri, D. V. Voronine, F. Šanda and S. Mukamel, *Chem. Rev.*, 2009, **109**, 2350–2408.

68 T. Meier, V. Chernyak and S. Mukamel, *J. Chem. Phys.*, 1997, **107**, 8759–8780.

69 W. M. Zhang, T. Meier, V. Chernyak and S. Mukamel, *J. Chem. Phys.*, 1998, **108**, 7763–7774.

Table 1 Calculated IR frequencies and intensities of $H_2PO_4^-$ (in cm^{-1}): top - mean instantaneous frequencies from hybrid QM/MM trajectory; middle- $H_2PO_4^-$ × 7 H_2O cluster on *VSCF/VCI* / DFT(PBE0)[a] level of theory; bottom - $H_2PO_4^-$ × 7 H_2O on *VSCF/VCI* / DFT(M05-2X)[b] level of theory; Basis: 6-311++G(d,p), [c] VSCF (VCI) level of theory
diagonal anharmonicity: $\Delta_{20} = 2 * \nu_{VSCF/VCI}(v{=}0\rightarrow1)$ - $\nu_{VSCF/VCI}(v{=}0\rightarrow2)$.

Model	Mode	H.O.	Diagonal	VSCF	Δ_{20}	VCI	Δ_{20}	Int. [a.u.] [c]
$H_2PO_4^-$ *solv.* (QMMM):								
	δ_{AS}(P-$(OH)_2$)	1249.4						
	δ_S(P-$(OH)_2$)	1224.5						
	$\nu_{AS}(PO_2)$	1158.0						
	$\nu_S(PO_2)$	1069.0						
	ν_{AS}(P-$(OH)_2$)	923.2						
$H_2PO_4^-$×7H_2O:[a]								
	$\nu_{AS}((OH)_2)$	3575.5	3449.4	3372.8	134.6	3403.0	120.3	903.9 (698.5)
	$\nu_S((OH)_2)$	3437.8	3266.4	3220.1	219.5	3232.8	216.1	626.1 (636.9)
	δ_{AS}(P-$(OH)_2$)	1258.2	1276.4	1250.8	0.9	1242.1	8.4	214.0 (184.8)
	δ_S(P-$(OH)_2$)	1237.0	1264.5	1230.4	-4.1	1218.1	26.5	178.7 (186.6)
	$\nu_{AS}(PO_2)$	1135.1	1141.5	1126.1	7.3	1119.0	10.9	276.3 (300.1)
	$\nu_S(PO_2)$	1056.3	1054.7	1047.2	5.3	1043.1	4.5	288.5 (267.6)
	ν_{AS}(P-$(OH)_2$)	927.3	933.3	930.4	3.3	929.1	3.0	416.0 (421.4)
	δ(O=P=O)	492.5	496.7	506.7	-2.6	506.0	-7.2	52.8 (49.0)
$H_2PO_4^-$×7H_2O:[b]								
	$\nu_{AS}((OH)_2)$	3580.3	3464.7	3396.1	145.8	3428.2	130.0	926.0 (708.5)
	$\nu_S((OH)_2)$	3437.0	3293.0	3263.0	241.7	3274.8	236.6	640.9 (582.2)
	δ_{AS}(P-$(OH)_2$)	1262.3	1281.6	1242.6	2.2	1233.5	4.2	233.8 (204.6)
	δ_S(P-$(OH)_2$)	1245.5	1260.4	1207.2	-9.7	1190.7	23.2	181.7 (222.8)
	$\nu_{AS}(PO_2)$	1137.4	1144.4	1129.8	8.5	1122.8	10.2	290.6 (327.4)
	$\nu_S(PO_2)$	1064.8	1067.4	1056.2	4.9	1052.6	6.4	308.8 (288.0)
	ν_{AS}(P-$(OH)_2$)	937.8	943.0	933.3	2.7	931.6	2.4	460.0 (463.4)
	δ(O=P=O)	502.8	506.2	515.0	-2.5	514.0	-9.1	58.9 (40.9)